# Understanding the ferromagnetic-insulator phase in manganites through a localized band model

Sanjukta Paul and Sudhakar Yarlagadda
*CMP Division, Saha Institute of Nuclear Physics, HBNI, Kolkata 700064, India*

(Received 7 June 2020; revised 21 November 2020; accepted 12 January 2021; published 25 January 2021)

Understanding the coexistence of ferromagnetism and insulating behavior in manganites is an unsolved problem. We propose a localized band model involving effective intermediate-range electron-electron (electron-hole) repulsion (attraction) generated by cooperative electron-phonon interaction. A double-exchange mechanism, involving holes virtually hopping to nearest neighbors and back, produces magnetic polarons in an antiferromagnetic environment; when these magnetic polarons coalesce and percolate the system, we get a ferromagnetic insulator. Ferromagnetism gets more pronounced when the concentration of holes (doping) increases or when the ratio of hopping to polaronic-energy dominates over the ratio of superexchange-coupling to hopping.

DOI: 10.1103/PhysRevB.103.035140

## I. INTRODUCTION

Perovskite oxides, such as manganites, display a variety of orbital, charge, and spin orders when the parent oxide is doped. While significant progress has been made in characterizing most of the phenomena in bulk-doped materials, the understanding pertaining to ferromagnetic insulator (FMI) is still elusive. FMIs, inherently rare, are vital for many new magnetic devices, such as dissipationless quantum-spintronic devices, magnetic tunnel junctions, and solid-state quantum computers [1]. The doped alloy $T_{1-x}D_xMnO_3$ (where $T$ refers to trivalent rare-earth elements such as La, Pr, Nd, etc., and $D$ refers to divalent alkaline elements Sr, Ca, etc.) is an antiferromagnet when $x > 0.5$ with the nature of the antiferromagnet (i.e., A-, C-, CE-, or G-type antiferromagnet) depending on the compound and the dopant value $x$ [2–4]. Contrastingly, for $x < 0.5$, $T_{1-x}D_xMnO_3$ is an intriguing ferromagnetic insulator (FMI) at smaller values of $x$ (i.e., $0.1 \lesssim x \lesssim 0.2$) [5–7] and is a ferromagnetic metal at higher dopings in the manganite systems $La_{1-x}Sr_xMnO_3$, $La_{1-x}Ca_xMnO_3$, $Pr_{1-x}Sr_xMnO_3$, and $Nd_{1-x}Sr_xMnO_3$.

For modeling the diverse orderings and for exploiting the functionality in these transition-metal oxides, one needs effective Hamiltonians for various types of interactions. Although the importance of strong electron-phonon interaction (EPI) has been pointed out much earlier [8] and significant progress has been made some time ago in numerically treating electron-phonon interaction in sizable systems [9], the treatment of cooperative EPI (involving quantum phonons) was accomplished analytically only more recently in two dimensions (2D) [10]. It has been demonstrated analytically in Ref. [10] that introducing cooperative effects, when EPI is strong, produces nearest-neighbor (NN), next-nearest-neighbor (NNN), and next-to-next-nearest-neighbor (NNNN) interactions. Furthermore, incorporating spin-spin interactions along with cooperative strong EPI is still an unsolved analytic problem.

As regards experiments pertaining to ferromagnetic-insulating regions, while some suggested microscopically homogeneous electronic properties [11–13], others speculate that coexistence of ferromagnetic metallic phases and antiferromagnetic insulating phases leads to an inhomogeneous ferromagnetic insulating state [14,15].

We will now argue, without considering any specific model, that ferromagnetic-insulating phases are possible at low doping in manganites by presenting below general theoretical points based on the essential features of manganites.

(1) Kinetic energy (KE) is quite small at low doping because bare hopping is small (caused by lower tolerance factor [16], cation disorder, compatibility of distortions [17]) and the electron-phonon coupling is strong. The electrons are rendered essentially immobile and site localized due to spatial disorder.

(2) Potential energy (from repulsive interactions, due to cooperative EPI, that are intermediate range, i.e., NN, NNN, NNNN, etc.) is much larger than KE. The ground state is classical and the state of the system can be expressed by a single state in the occupation number basis with number density at each site either 1 or 0.

The fact that electrons are essentially site localized also follows from the treatment in Ref. [18]; then, only a localized polaronic band is relevant and the upper wide band cannot overlap with the lower narrow polaronic band.

Furthermore, a simple type of phase-separated state with ferromagnetic droplets (each containing one carrier) in an antiferromagnetic matrix was shown to be possible in Ref. [19]. The mobility of these magnetic polarons is low and they are easily localized by disorder and Coulomb interactions.

Thus, the potential energy determines the charge and spin order.

(3) Because of cooperative strong EPI, a NN electron-hole pair has a strong ferromagnetic interaction [$t^2\cos^2(\theta/2)/(2E_{JT})$ with $E_{JT}$ being the cooperative Jahn-Teller energy, $t$ the hopping term between the NN sites, and $\theta$ the angle between the NN core spins]. Hence, a robust ferromagnetic cluster is produced in the vicinity of a hole.

 

(4) Our model for magnetic interaction applies to manganites with low density of localized holes. In regions away from the holes, the cooperative EPI retains essentially the same orbital texture as in the undoped manganite. As a result, in regions without holes, the magnetic interaction is A-AFM just as in the undoped manganite. As regards the regions with holes, since the holes are site localized, the holes only virtually hop to a NN site and back and thus produce ferromagnetic coupling between nearest neighbors. This ferromagnetic coupling, between NN electron-hole pair, is much stronger than the A-AFM coupling.

(5) Presence of site-localized holes produces FMI clusters due to formation of magnetic polarons. A hole will polarize NN electrons (and realistically speaking, NNN and NNNN electrons as well) through virtual hopping, thereby producing a magnetic polaron. A collection of interacting magnetic polarons will produce a FMI region. It is interesting to note that FMI regions are present at moderate doping in manganites that are narrow band ($Pr_{1-x}Ca_xMnO_3$), intermediate band ($La_{1-x}Ca_xMnO_3$), and wide band ($La_{1-x}Sr_xMnO_3$).

The rest of the paper is organized as follows. In Sec. II, invoking cooperative electron-phonon-interaction physics, we obtain the effective Hamiltonian that is employed to understand the FMI phase in manganites. Next, in Sec. III, we outline our calculation procedure involving the Monte Carlo technique. We use this procedure to simulate charge and spin configurations and obtain the magnetization as a function of various parameters. Then, in Sec. IV, we discuss our results obtained for systems with different hoppings at various temperatures and dopings. Lastly, in Sec. V, we conclude and offer some perspectives.

## II. EFFECTIVE HAMILTONIAN

In this section, we focus on the analytical treatment of the effective Hamiltonian which will be used for numerical simulation. We are working with a 2D version of the perovskite manganite system which has Mn-O-Mn bonds along the $x$ and $y$ directions. We have $e_g$ electrons (or holes) interacting with the oxygen atoms. We have restricted our analysis to a system of fermions interacting with the oxygens in the $xy$ plane via cooperative breathing mode and with the out-of-plane ($z$ direction) oxygens through noncooperative breathing mode as depicted in Fig. 1.

Apart from the itinerant $e_g$ electrons, we also have a $t_{2g}$ localized core-spin background with spin $S = \frac{3}{2}$ at each site. Thus, the Hamiltonian of such a system has five contributions: the kinetic energy of the fermions, the fermion-lattice coupling energy, the lattice energy, the spin-spin interaction energy, and the fermion-disorder interaction energy:

$$H = H_{\rm KE} + H_{\rm int} + H_{\rm lat} + H_{\rm SE} + H_{\rm dis}. \tag{1}$$

Here,

$$H_{\rm KE} = -t \sum_{i,j} \left[ \cos\left(\frac{\theta_{i,j;i+1,j}}{2}\right) d^{\dagger}{}_{i+1,j} d_{i,j} + \cos\left(\frac{\theta_{i,j;i,j+1}}{2}\right) d^{\dagger}{}_{i,j+1} d_{i,j} + \text{H.c.} \right], \tag{2}$$

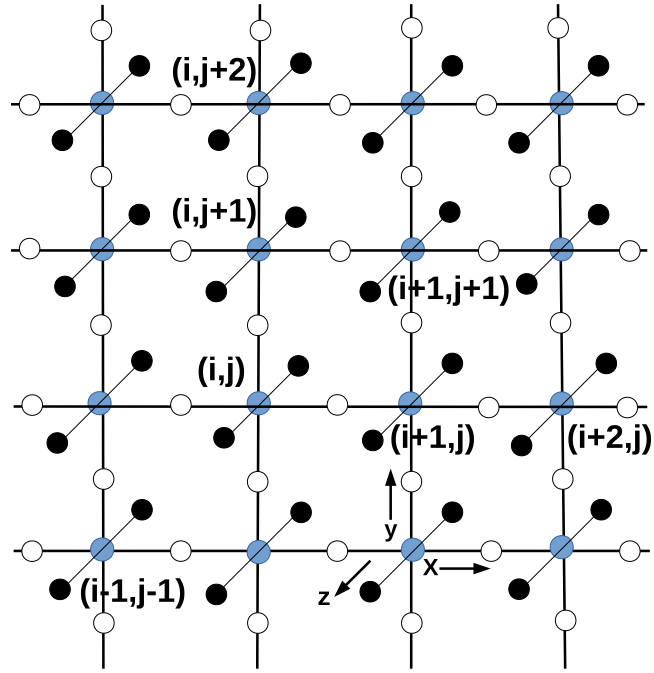


FIG. 1. Schematic diagram for a 2D cooperative breathing mode (CBM) system. Hopping sites for holes are represented by blue solid circles, in-plane oxygen atoms (participating in the CBM) by black empty circles, and noncooperative out-of-plane oxygen atoms by solid black circles.

and $d_{i,j}$ ($d^{\dagger}{}_{i,j}$) represents the annihilation (creation) operator for the fermion at site $(i, j)$; $t$ is the hopping amplitude for the fermion; the hopping process is modified by $\theta$, the angle between two localized $S = \frac{3}{2}$ spins at NN sites [20,21]. The second term represents the interaction between the fermions and the quantum phonons in the system and is expressed as [10]

$$H_{\rm int} = -g\omega_0 \sum_{i,j} \{(a^{\dagger}{}_{x;i,j} + a_{x;i,j})(n_{i,j} - n_{i+1,j}) + (b^{\dagger}{}_{y;i,j} + b_{y;i,j})(n_{i,j} - n_{i,j+1}) + \gamma(c^{\dagger}{}_{z;i,j} + c_{z;i,j})n_{i,j}\}, \tag{3}$$

where $\gamma = \sqrt{2}$, $g$ is the electron-phonon coupling constant, $\omega_0$ is the optical-phonon frequency, and $n_{i,j} = d^{\dagger}_{i,j} d_{i,j}$. The displacement of the oxygen atom that is adjacent to the site $(i, j)$ in the positive $x$ ($y$) direction is given by $\frac{(a^{\dagger}{}_{x;i,j} + a_{x;i,j})}{\sqrt{2m\omega_0}}$ ($\frac{(b^{\dagger}{}_{y;i,j} + b_{y;i,j})}{\sqrt{2m\omega_0}}$). In the $z$ direction, the relative displacement of the two oxygen atoms next to site $(i, j)$ is denoted by $\frac{(c^{\dagger}{}_{z;i,j} + c_{z;i,j})}{\sqrt{2m\omega_0/2}}$ with $m/2$ being the reduced mass of the oxygen pair. Next, the lattice energy due to quantum harmonic oscillators is given by

$$H_{\rm lat} = \sum_{i,j} (a^{\dagger}{}_{x;i,j} a_{x;i,j} + b^{\dagger}{}_{y;i,j} b_{y;i,j} + \eta c^{\dagger}{}_{z;i,j} c_{z;i,j}), \tag{4}$$

with $\eta$ being set to be 1. The form of $H_{\rm lat}$ and $H_{\rm int}$ corresponds to treating cooperative breathing mode in two dimensions and considering quantum phonons. Including cooperative

Jahn-Teller effect (by considering quantum phonons) and extending it to three dimensions will significantly add to the difficulty of an analytic treatment without altering the essential physics and results. The last term in the Hamiltonian $H$ represents the interaction with disorder and is expressed as

$$H_{\rm dis} = \sum_{i,j} V_{i,j} n_{i,j}, \tag{5}$$

where $V_{i,j}$ is the potential due to spatial disorder.

Now, to arrive at an effective Hamiltonian which can be expressed solely in terms of fermionic operators, we take resort to an analytic approach similar to that described in Ref. [10]. This approach involves a duality transformation which converts a difficult strong-coupling problem to a tractable weak-coupling one. For large electron-phonon coupling, the above Hamiltonian $H$ is subject to a canonical transformation (i.e., modified Lang-Firsov transformation) to produce an unperturbed part $H_0$ and the perturbation term $H_1$. To obtain an effective Hamiltonian, we perform second-order perturbation theory (as in Refs. [10,22]) and obtain

$$\begin{aligned} H_{\rm eff} &= -E_p \sum_{i,j} n_{i,j} + 2V_p \sum_{i,j} (n_{i,j} n_{i+1,j} + n_{i,j} n_{i,j+1}) \\ &+ t e^{-(E_p+V_p)/\omega_0} \sum_{i,j} \Bigg[ \cos\left(\frac{\theta_{i,j;i+1,j}}{2}\right) d^\dagger_{i+1,j} d_{i,j} \\ &+ \cos\left(\frac{\theta_{i,j;i,j+1}}{2}\right) d^\dagger_{i,j+1} d_{i,j} + \text{H.c.} \Bigg] \\ &+ H^{(2)} + H_{\rm SE} + \sum_{i,j} V_{i,j} n_{i,j}, \end{aligned} \tag{6}$$

where the polaronic energy $E_p = (4+\gamma^2) g^2 \omega_0 = 6 g^2 \omega_0$ and the nearest-neighbor repulsion energy $V_p = g^2 \omega_0$; the second-order perturbation theory yields the term $H^{(2)}$. The small parameter of the perturbation theory is $\sim [\frac{t^2}{2(E_p+V_p)\omega_0}]^{\frac{1}{2}}$ as derived in Ref. [23]. Now, the effective hopping term $t e^{-(E_p+V_p)/\omega_0} \ll \omega_0$ and $V_{i,j} \ll E_p$. For large $g$, the effective hopping term will be very small compared to the other terms in $H_{\rm eff} - H_{\rm SE}$. Hence, we ignore the kinetic energy of the system and treat the system as made up of carriers that are localized due to weak spatial disorder. Then, we are justified in treating the problem entirely classically with physics being governed by the dominant potential energy terms in the effective Hamiltonian.

Then, we can rewrite Eq. (6) as

$$H_{\rm eff} = 2V_p \sum_{i,j} (n_{i,j} n_{i+1,j} + n_{i,j} n_{i,j+1}) + H^{(2)} + H_{\rm SE}. \tag{7}$$

This formalism omits a constant energy term $-E_p \sum_{i,j} n_{i,j}$ in the effective Hamiltonian because it does not change the physics of the problem. The convention we will use throughout the paper is that $n_{i,j}$ will represent number density of a hole at the lattice site $(i, j)$ of the system. To calculate $H^{(2)}$, we go through an algebra similar to that mentioned in Appendix A of Ref. [10] and arrive at a nearest-neighbor repulsion term corresponding to the process where a particle in 2D virtually hops to its NN and comes back. When a hole at site $(i, j)$ hops to its NN site, such as $(i+1, j)$, and comes back, we need to keep track of the occupancy of the three relevant nearest-neighbor sites of the intermediate site $(i+1, j)$, i.e., the occupancy of the three sites $(i+2, j)$, $(i+1, j+1)$, and $(i+1, j-1)$. Depending on how many of these three sites are filled, the coefficient for the hopping-and-returning process will be modified.

Clearly, there are four such possibilities for the coefficients and they will be considered below.

### A. Three NN sites of the intermediate site are filled by electrons

In Fig. 2, when the intermediate site containing an electron is surrounded by a hole and three electrons, we depict the hole at site $(i, j)$ hopping to its NN site (the intermediate site) and returning back. The intermediate site can be any of the four NNs of the originating site $(i, j)$. A schematic view of the four possibilities is shown in Fig. 2.

When a hole is at $(i, j)$, its energy is equal to $-E_p$. The oxygen atoms on both the sides of the initial site are attracted by the hole on the initial site and hence are pulled towards the hole. When the hole virtually hops to the intermediate site, its energy is equal to $E_p + 2V_p$ because the oxygen distortions remain unchanged; in the energy of the intermediate state, $E_p$ arises due to the distortion without the hole whereas the extra energy $2V_p$ (equal in magnitude to the NN repulsion energy between two holes) results due to displacing the oxygen atoms towards the initial site and away from the hole. Hence, change in the energy when the hole jumps from the originating site to the intermediate site is equal to $2E_p + 2V_p$. Thus, the coefficient of the second-order perturbation term turns out to be $\frac{t^2}{2E_p+2V_p}$ and the contribution to $H^{(2)}$ from all the possibilities corresponding to Fig. 2 is given by

$$\begin{aligned} H^{(2)}_1 = -\frac{t^2}{(2E_p+2V_p)} \sum_{i,j} \Bigg[ & \cos^2\left(\frac{\theta_{i,j;i+1,j}}{2}\right) \{n_{i,j}(1-n_{i+1,j})(1-n_{i+2,j})(1-n_{i+1,j+1})(1-n_{i+1,j-1})\} \\ & + \cos^2\left(\frac{\theta_{i,j;i-1,j}}{2}\right) \{n_{i,j}(1-n_{i-1,j})(1-n_{i-2,j})(1-n_{i-1,j+1})(1-n_{i-1,j-1})\} \\ & + \cos^2\left(\frac{\theta_{i,j;i,j-1}}{2}\right) \{n_{i,j}(1-n_{i,j-1})(1-n_{i,j-2})(1-n_{i-1,j-1})(1-n_{i+1,j-1})\} \\ & + \cos^2\left(\frac{\theta_{i,j;i,j+1}}{2}\right) \{n_{i,j}(1-n_{i,j+1})(1-n_{i,j+2})(1-n_{i-1,j+1})(1-n_{i+1,j+1})\} \Bigg]. \end{aligned} \tag{8}$$

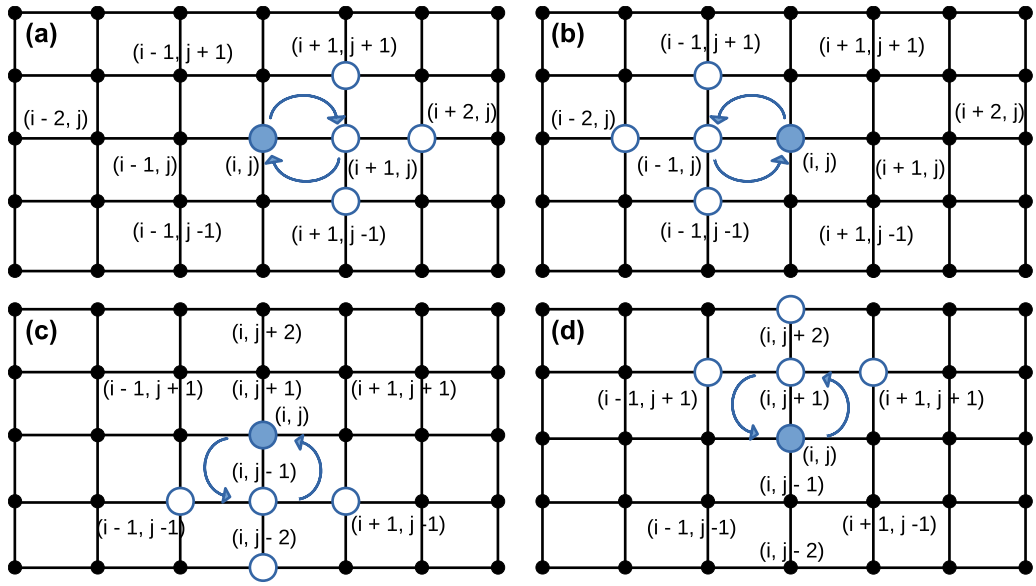


FIG. 2. Schematic diagram for the four possibilities of a hole, at an originating site $(i, j)$, hopping to its NN site (the intermediate site) and coming back (when three NN sites of the intermediate site are occupied by electrons): (a) hole at $(i, j)$ hops to its right NN at $(i + 1, j)$ and comes back; (b) hole at $(i, j)$ jumps to its left NN at $(i - 1, j)$ and returns back; (c) hole at $(i, j)$ jumps to its downward NN at $(i, j - 1)$ and comes back; (d) hole at $(i, j)$ hops to its upper NN at $(i, j + 1)$ and returns. A hole is represented by a blue solid circle and a particle (i.e., electron) by a blue empty circle. All lattice sites that are not relevant to the consideration are represented by black solid circles.

### B. Any two of NN sites of the intermediate site is filled

In Fig. 3, we depict the three possibilities corresponding to a hole at a site $(i, j)$ hopping to its NN site (the intermediate site) and returning; here, any two of the NN sites of the intermediate site are occupied by electrons. Henceforth, we will show all the counterpart processes of Fig. 2(a) (considering these as representative diagrams) for various possibilities. Similar processes, which will not be shown here, also occur for Figs. 2(b), 2(c), and 2(d).

When the hole virtually hops to the intermediate site, its energy is equal to $E_p + 4V_p$; here, an extra repulsion of $2V_p$ is generated due to the occupancy of any one of the NN sites of the intermediate site by a hole. Then, the coefficient of the

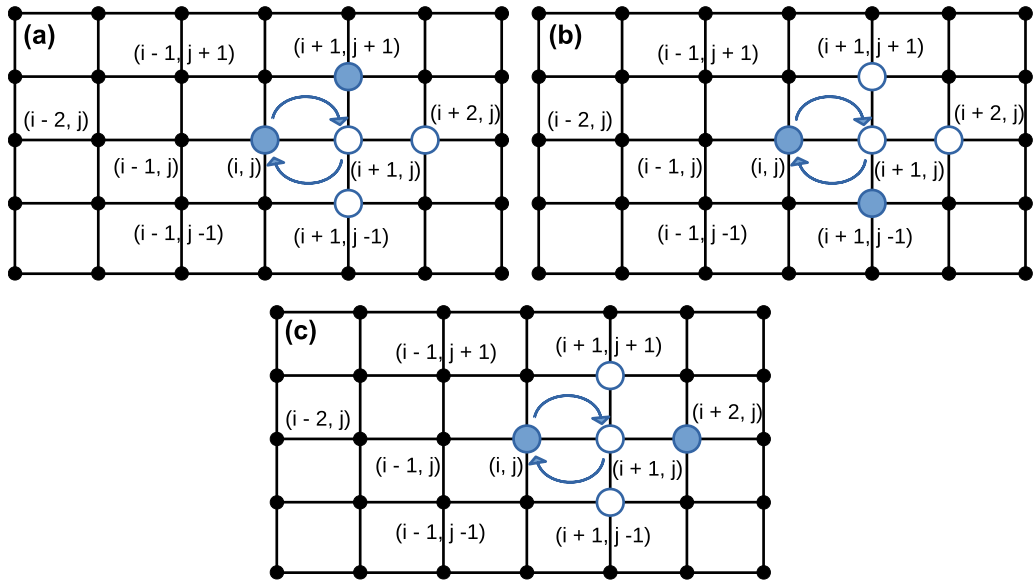


FIG. 3. Schematic diagram for a hole at an originating site $(i, j)$ hopping to its NN site (the intermediate site) and returning back (when any two of the NN sites of the intermediate site are occupied by electrons). Representation of a hole at $(i, j)$ jumping to its right NN at $(i + 1, j)$ and coming back when holes occupy (a) right and downward NNs of the intermediate site; (b) right and upward NNs of the intermediate site; (c) upward and downward NNs of the intermediate site. A hole is depicted by a blue solid circle and a particle by a blue empty circle. All lattice sites that are not relevant to the consideration are represented by black solid circles.

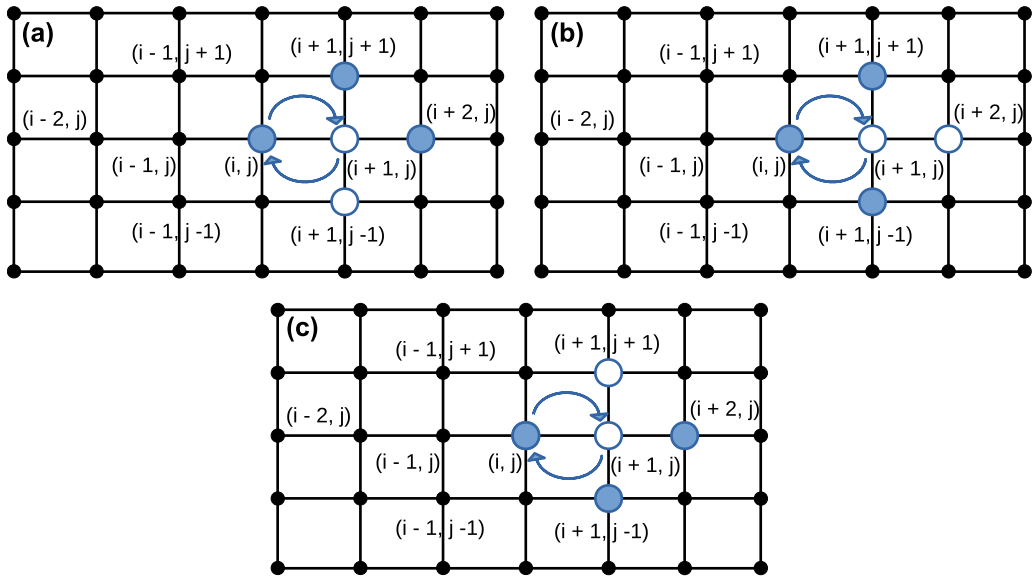


FIG. 4. Schematic diagram for a hole at an originating site $(i, j)$ hopping to its NN site (the intermediate site) and coming back (when any one of the NN sites of the intermediate site is occupied by an electron). Depiction of a hole at $(i, j)$ jumping to its right NN at $(i + 1, j)$ and coming back when a particle occupies (a) downward NN of the intermediate site; (b) right NN of the intermediate site; (c) upward NN of the intermediate site. A hole is represented by a blue solid circle whereas a particle by a blue empty circle. All lattice sites that are not relevant to the consideration are indicated by black solid circles.

second-order perturbation term is $\frac{t^2}{2E_p+4V_p}$ and the contribution to $H^{(2)}$ from all the possibilities, similar to and corresponding to Fig. 3, is given by

$$\begin{aligned}
H_2^{(2)} = -\frac{t^2}{(2E_p+4V_p)}\sum_{i,j}\Bigg[&\cos^2\left(\frac{\theta_{i,j;i+1,j}}{2}\right)\{n_{i,j}(1-n_{i+1,j})n_{i+2,j}(1-n_{i+1,j+1})(1-n_{i+1,j-1})\\
&+n_{i,j}(1-n_{i+1,j})(1-n_{i+2,j})n_{i+1,j+1}(1-n_{i+1,j-1})+n_{i,j}(1-n_{i+1,j})(1-n_{i+2,j})(1-n_{i+1,j+1})n_{i+1,j-1}\}\\
&+\cos^2\left(\frac{\theta_{i,j;i-1,j}}{2}\right)\{n_{i,j}(1-n_{i-1,j})n_{i-2,j}(1-n_{i-1,j+1})(1-n_{i-1,j-1})\\
&+n_{i,j}(1-n_{i-1,j})(1-n_{i-2,j})n_{i-1,j+1}(1-n_{i-1,j-1})+n_{i,j}(1-n_{i-1,j})(1-n_{i-2,j})(1-n_{i-1,j+1})n_{i-1,j-1}\}\\
&+\cos^2\left(\frac{\theta_{i,j;i,j-1}}{2}\right)\{n_{i,j}(1-n_{i,j-1})n_{i,j-2}(1-n_{i-1,j-1})(1-n_{i+1,j-1})\\
&+n_{i,j}(1-n_{i,j-1})(1-n_{i,j-2})n_{i-1,j-1}(1-n_{i+1,j-1})+n_{i,j}(1-n_{i,j-1})(1-n_{i,j-2})(1-n_{i-1,j-1})n_{i+1,j-1}\}\\
&+\cos^2\left(\frac{\theta_{i,j;i,j+1}}{2}\right)\{n_{i,j}(1-n_{i,j+1})n_{i,j+2}(1-n_{i-1,j+1})(1-n_{i+1,j+1})\\
&+n_{i,j}(1-n_{i,j+1})(1-n_{i,j+2})n_{i-1,j+1}(1-n_{i+1,j+1})+n_{i,j}(1-n_{i,j+1})(1-n_{i,j+2})(1-n_{i-1,j+1})n_{i+1,j+1}\}\Bigg].
\end{aligned} \tag{9}$$

### C. Any one of NN sites of the intermediate site has an electron

In Fig. 4, three possibilities have been shown for the process where a hole jumps to an intermediate site and comes back; here, any one of the NNs of the intermediate site is filled by an electron. Extending the logic given above to the present case, the coefficient of the second-order perturbation term is $\frac{t^2}{2E_p+6V_p}$ and the contribution to $H^{(2)}$ from all the possibilities, similar to and corresponding to Fig. 4, is given by

$$\begin{aligned}
H_3^{(2)} = -\frac{t^2}{(2E_p+6V_p)}\sum_{i,j}\Bigg[&\cos^2\left(\frac{\theta_{i,j;i+1,j}}{2}\right)\{n_{i,j}(1-n_{i+1,j})n_{i+2,j}n_{i+1,j+1}(1-n_{i+1,j-1})\\
&+n_{i,j}(1-n_{i+1,j})(1-n_{i+2,j})n_{i+1,j+1}n_{i+1,j-1}+n_{i,j}(1-n_{i+1,j})n_{i+2,j}(1-n_{i+1,j+1})n_{i+1,j-1}\}
\end{aligned}$$

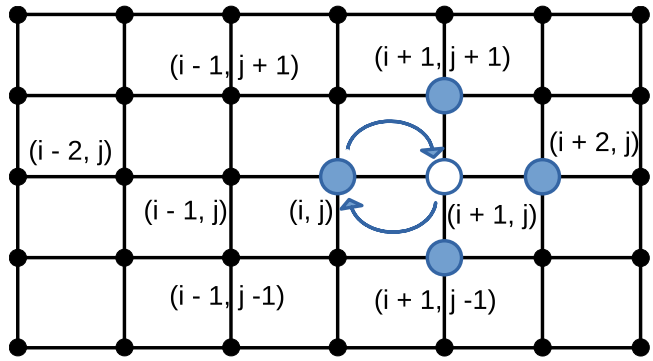


FIG. 5. Schematic diagram for a hole at an originating site $(i, j)$ hopping to its NN site (the intermediate site) and coming back (when all the other three NN sites of the intermediate site are occupied by electrons). Representation of a hole at $(i, j)$ jumping to its right NN at $(i + 1, j)$ and coming back. A hole is represented by a blue solid circle and a particle by a blue empty circle. All lattice sites irrelevant to the analysis are represented by black solid circles.

$$
\begin{aligned}
&+\cos^2\left(\frac{\theta_{i,j;i-1,j}}{2}\right)\{n_{i,j}(1-n_{i-1,j})n_{i-2,j}n_{i-1,j+1}(1-n_{i-1,j-1})\\
&+n_{i,j}(1-n_{i-1,j})(1-n_{i-2,j})n_{i-1,j+1}n_{i-1,j-1}+n_{i,j}(1-n_{i-1,j})n_{i-2,j}(1-n_{i-1,j+1})n_{i-1,j-1}\}\\
&+\cos^2\left(\frac{\theta_{i,j;i,j-1}}{2}\right)\{n_{i,j}(1-n_{i,j-1})n_{i,j-2}n_{i-1,j-1}(1-n_{i+1,j-1})\\
&+n_{i,j}(1-n_{i,j-1})(1-n_{i,j-2})n_{i-1,j-1}n_{i+1,j-1}+n_{i,j}(1-n_{i,j-1})n_{i,j-2}(1-n_{i-1,j-1})n_{i+1,j-1}\}\\
&+\cos^2\left(\frac{\theta_{i,j;i,j+1}}{2}\right)\{n_{i,j}(1-n_{i,j+1})n_{i,j+2}(1-n_{i-1,j+1})n_{i+1,j+1}\\
&+n_{i,j}(1-n_{i,j+1})(1-n_{i,j+2})n_{i-1,j+1}n_{i+1,j+1}+n_{i,j}(1-n_{i,j+1})n_{i,j+2}n_{i-1,j+1}(1-n_{i+1,j+1})\}\Bigg].
\end{aligned}
\tag{10}
$$

### D. All the NN sites of the intermediate site have holes

.

Here, for the situation where all the NN sites of the intermediate site have holes, we depict in Fig. 5 a hole hopping to an intermediate site and coming back. Here, the coefficient of the second-order perturbation term is $\frac{t^2}{2E_p+8V_p}$ and the contribution to $H^{(2)}$ from all the possibilities, similar to and corresponding to Fig. 5, is given by

$$
\begin{aligned}
H_4^{(2)} = -\frac{t^2}{(2E_p+8V_p)}\sum_{i,j}\Bigg[&\cos^2\left(\frac{\theta_{i,j;i+1,j}}{2}\right)\{n_{i,j}(1-n_{i+1,j})n_{i+2,j}n_{i+1,j+1}n_{i+1,j-1}\}\\
&+\cos^2\left(\frac{\theta_{i,j;i-1,j}}{2}\right)\{n_{i,j}(1-n_{i-1,j})n_{i-2,j}n_{i-1,j+1}n_{i-1,j-1}\}\\
&+\cos^2\left(\frac{\theta_{i,j;i,j-1}}{2}\right)\{n_{i,j}(1-n_{i,j-1})n_{i,j-2}n_{i-1,j-1}n_{i+1,j-1}\}\\
&+\cos^2\left(\frac{\theta_{i,j;i,j+1}}{2}\right)\{n_{i,j}(1-n_{i,j+1})n_{i,j+2}n_{i-1,j+1}n_{i+1,j+1}\}\Bigg].
\end{aligned}
\tag{11}
$$

From the contributions $H_1^{(2)}$, $H_2^{(2)}$, $H_3^{(2)}$, and $H_4^{(2)}$ obtained above, we express $H^{(2)}$ as

$$
H^{(2)} = H_1^{(2)} + H_2^{(2)} + H_3^{(2)} + H_4^{(2)}. \tag{12}
$$

Lastly, the superexchange [24] term $H_{SE}$ generates A-AFM spin-spin exchange in manganites such as $LaMnO_3$ and is given by

$$
H_{SE} = -J_{xy}\sum_{\langle i,j\rangle_{xy}}\cos(\theta_{ij}) + J_z\sum_{\langle i,j\rangle_z}\cos(\theta_{ij}). \tag{13}
$$

Here, we mention that the spins of the $t_{2g}$ electrons, being $S = \frac{3}{2}$, can be treated as classical spin vectors. Furthermore,

it is important to note that, while the range of charge-charge interaction is as far as NNNN, the range of spin-spin interaction is only NN. The effective electron-electron interaction is obtained from electron-phonon interaction by performing perturbation theory and eliminating the phonon degrees of freedom as shown in Appendix B of Ref. [10]. On the other hand, the spin-spin interactions are due to double exchange and superexchange; consequently, the range of the spin-spin interactions is determined by the range of the nearest-neighbor hopping. If cooperative effects are ignored, then $V_p = 0$ and, similar to the range of the spin-spin interaction, we would have the range of the charge-charge interaction to be nearest neighbor only.

## III. CALCULATION PROCEDURE

For a numerical study, we consider a 2D lattice with periodic boundary conditions in both directions. We treat the problem fully classically using the effective Hamiltonian, comprising of the effective electron-phonon interaction (the charge-spin-coupled term) and the superexchange interaction (the spin-spin interaction term), as given by Eq. (7). We use classical Monte Carlo technique and make use of the standard Metropolis algorithm to update the charge configuration as well as the spin configuration of the system. We follow a two-step procedure to arrive at the final charge and spin configurations.

First, to deal with problem of charge configurations that correspond to local minima which are close in energy, we resort to simulated annealing for the charge degrees of freedom only. The spin variables are kept frozen since the energy scale for the charge interactions is much higher than the energy scale for superexchange interactions. Since we are working with low hole densities (i.e., between 0.1 and 0.3), a large number of degenerate states will appear in the charge spectrum. In order to obtain maximum number of such degenerate configurations, we employ a three-step procedure at each temperature of the simulated annealing process to obtain the optimized charge configurations. The primary step is a "single-particle-exchange" process where we choose any two sites at a time, one sequentially and the other randomly, and exchange their number-density values provided they differ by 1. Physically, we exchange a particle at a site with a hole at any other site. The secondary step is a "general-two-particle-exchange" process where any two random sites are selected with both being occupied by particles and then their occupants are exchanged with another pair of randomly chosen sites both containing holes. Thus, we actually exchange two particles with two holes at a time. The final step, a "plaquette-exchange" process, is a special case of the "general-two-particle-exchange" mechanism. Here, plaquettes are chosen sequentially; if the difference in number densities between the two diagonal pairs is 2, then the number densities of the diagonals are exchanged. At a particular temperature, to arrive at the final lowest-energy charge configuration at that temperature using Monte Carlo technique, an initial random charge configuration (with a fixed number of particles) first goes through $4 \times 10^5$ steps of "single-particle-exchange"; then, an equal number of steps involving "general-two-particle-exchange"; followed by 30 times the system size number "plaquette-exchange" steps.

Second, using the charge profile generated by the three-step process, we now optimize spin variables by taking an initial random spin configuration and updating through the Metropolis algorithm. The spins $\vec{S}_i$, being large in magnitude, are essentially classical spins with $\vec{S}_i = (\sin\theta_i \cos\phi_i, \sin\theta_i \sin\phi_i, \cos\theta_i)$. While updating the spins, we consider the full Hamiltonian $H_{\text{eff}}$ and consider both the charge and spin interaction energies. The $\cos(\theta)$ and $\phi$ values are binned to fix the orientation of the classical spin vector. We have allowed equally spaced 40 values of $\cos(\theta)$ in the interval $(-1, 1)$ and 80 values of $\phi$ in the usual range of $(0, 2\pi)$, thus totaling to 3200 different possibilities. A sweep involves visiting all the lattice sites sequentially and updating the spin orientation at each lattice site by the Metropolis algorithm. The equilibrium number of sweeps required for medium (higher) temperatures is around $15 \times 10^5$ ($6 \times 10^5$), while another $15 \times 10^5$ ($6 \times 10^5$) sweeps are required for the thermal averaging of the total magnetization of the system. It is to be noted that for low-hole concentrations, we have many degenerate states. We calculate the magnetization for typically 10 degenerate configurations. The degenerate states are chosen based on the charge optimization process only, fed to the full Hamiltonian $H_{\text{eff}}$ containing both charge and spin variables, and then energy is optimized to obtain the total magnetization of all such states. The magnetization/site of the system, that has been plotted, is the magnetization/site averaged over all the degenerate states for a particular filling of holes when spins are normalized to unity.

We study the system for the bare hopping parameter values $t = 0.2$ and 0.3 eV. Our calculations take the polaronic energy to be $E_p = 0.43$ eV and the nearest-neighbor repulsion energy to be $V_p = 0.07$ eV. Thus, we are in the regime of strong electron-phonon coupling characterized by $(E_p + V_p)/\omega_0 \gg 1$ with the optical phonon frequency $\omega_0$ value being given as 0.05 eV $< \omega_0 <$ 0.1 eV. The superexchange energy coefficient $J_z = 4.8$ meV [25,26]; thus, the superexchange energy is much smaller than the electron-hole pair ferromagnetic interaction coupling $[t^2/(2E_p + 2V_p)]$. Furthermore, the ferromagnetic coupling $J_{xy} = 1.4 \times J_z$. Thus, the charge configuration can be assumed to remain constant as the spins are optimized. The total magnetization of the system is computed at various temperatures, with the highest temperature being $T = 0.1t/k_B$ (i.e., about 330 K for $t = 0.3$ eV). Henceforth, $k_B$ will be set to unity for convenience. The lowest temperature on the other hand is $T = 0.001t$ (i.e., about 3 K for $t = 0.3$ eV) which is much smaller than $J_z$; thus, the system can be assumed to be in its ground state at $T = 0.001t$.

Here, we should comment that above $T = 0.03t$, the excited-state charge configurations also begin to contribute to the magnetization. In the Appendix we present the quality of the annealing, used to obtain optimized charge configurations of the system, through analyzing the energetics, as a function of temperature, in the Monte Carlo simulations.

## IV. RESULTS AND DISCUSSION

We consider a 2D lattice of dimensions $6 \times 12$ (i.e., with a total of 72 sites) with periodic boundary conditions in both

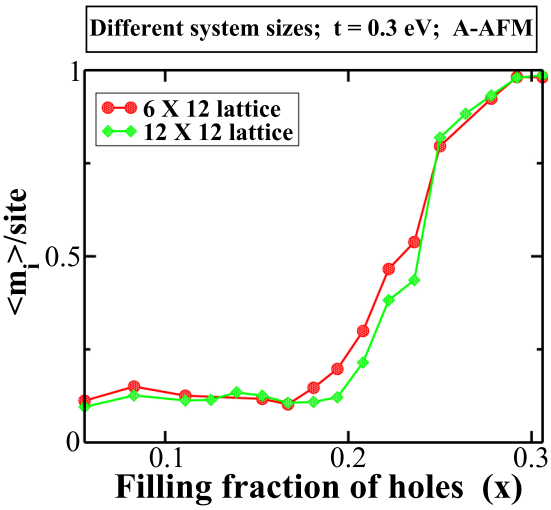


FIG. 6. Averaged per-site magnetization $\langle m_i \rangle$ (of spins normalized to unity) as a function of hole doping $x$ for two different lattices ($6 \times 12$ and $12 \times 12$) and for a fixed $T = 0.001t$.

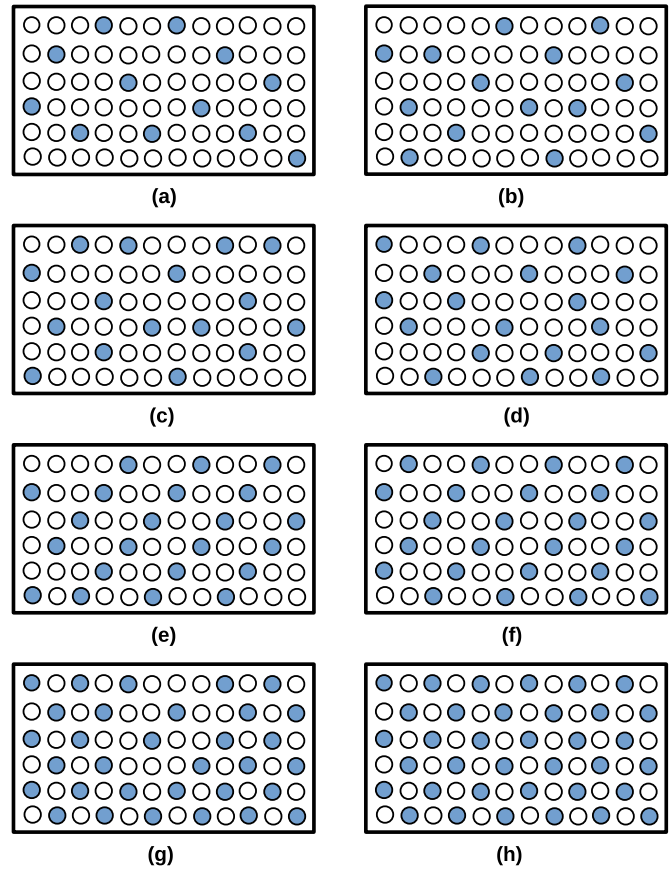


FIG. 7. Charge configurations in the ground state of a $6 \times 12$ lattice. An arbitrarily chosen degenerate ground state, involving 72 sites, for (a) 12 holes, (b) 14 holes, (c) 16 holes, (d) 18 holes, (e) 22 holes, (f) 24 holes (diagonal stripe order), (g) 32 holes, and (h) 36 holes.

directions; the number of rows being $l_x = 6$ and the number of columns being $l_z = 12$. Each site represents an Mn ion consisting of an electron and a positive charge center. We study the interplay between the electron-phonon interaction and the magnetic interaction of the spins [see Eq. (7)]. As stated earlier (in Sec. I), due to the the smallness of the kinetic energy in comparison to the potential energy, the problem is treated fully classically. Thus, the holes are site localized and the system can be represented by a single state in the occupation-number basis with the number density at each site being either 1 or 0. Hence, for strong electron-phonon interaction, we have a fully insulating system resembling a charge solid as shown in Fig. 7. Using the effective Hamiltonian in Eq. (7), we can simulate different observables in the system. We study the variation of the total magnetization of the system as a function of hole doping in the pure manganite sample.

### A. A-AFM background

The hopping value $t$ is varied to study the interplay between the electron-phonon interactions and the superexchange interactions in the system. The hole doping $x$ is varied as $0.1 \leqslant x \leqslant 0.3$. The magnetic profile still resembles that of an A-AFM system away from the holes; in the NN vicinity of a hole, the spins get polarized in the direction of the spin of the hole, thereby forming a magnetic polaron. For different hopping cases, the temperature variation of the total magnetization of the system is studied. We have also considered a 2D lattice with system size $12 \times 12$ and carried out the magnetization measurements. It shows qualitatively similar results as that of the $6 \times 12$ lattice as depicted in Fig. 6. However, the $12 \times 12$ system requires a running time which is $\simeq 5$ times that of the $6 \times 12$ case; also, the number of degenerate states for the $12 \times 12$ system is much more. Thus, dealing with the $12 \times 12$ case is computationally expensive. So, we conclude that $6 \times 12$ lattice can be considered to be representative for the $12 \times 12$ lattice and will be used for investigating the ferromagnet-insulator properties of the system.

At a very low-hole concentration $\simeq 0.1$ (i.e., 8 particles on a 72-site lattice), 8 holes get distributed among 12 columns such that NN as well as NNN and NNNN interactions are avoided. In most of the degenerate states, no two holes occupy the same column. Hence, we have site-localized holes in the system, polarizing their NN spins, giving rise to magnetic polarons that remain disconnected in the lattice. Due to the NN interaction $J_{xy}$, spins in a column try to align ferromagnetically; whereas $J_z (= J_{xy}/1.4)$ tends to order spins in a row antiferromagnetically. Thus, the ferromagnetic polarons and the ferromagnetic interaction in columns together give rise to an effective low-magnetization value (with a sizable fluctuation).

At each temperature, the value of magnetization is essentially unchanged between hole densities 8/72 and 12/72 ($\simeq 0.167$); this is because up to the filling 12/72, holes can still maintain to be noninteracting (on ignoring the superexchange) as can be seen in Fig. 7(a).

At temperatures $T < J_z$ ($= 0.016t$ for $t = 0.3$ eV and $= 0.024t$ for $t = 0.2$ eV), antiferromagnetic coupling between columns is effective and the system has low magnetization at low concentrations (i.e., $x \leqslant 12/72$). On increasing the temperature up to $T = J_z$, the effect of $J_z$ diminishes while the effect of ferromagnetic coupling $J_{xy} = 1.4J_z$ is more

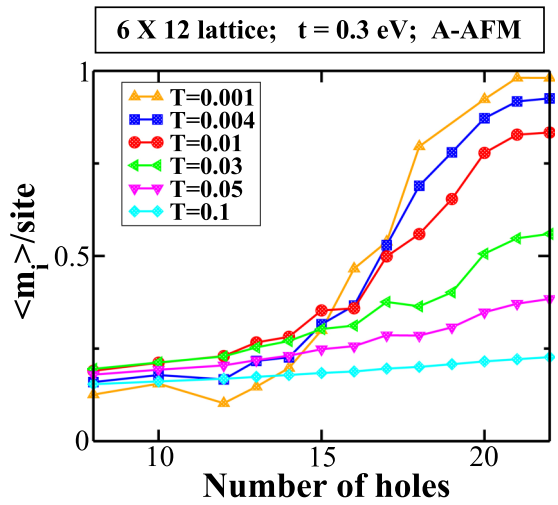


FIG. 8. Averaged per-site total magnetization $\langle m_i \rangle$ (of spins normalized to unity) as a function of the number of holes doped for a $6 \times 12$ lattice and for various temperatures (expressed in units of hopping parameter $t$). The background spin configuration is A-AFM type and hopping $t = 0.3$ eV.

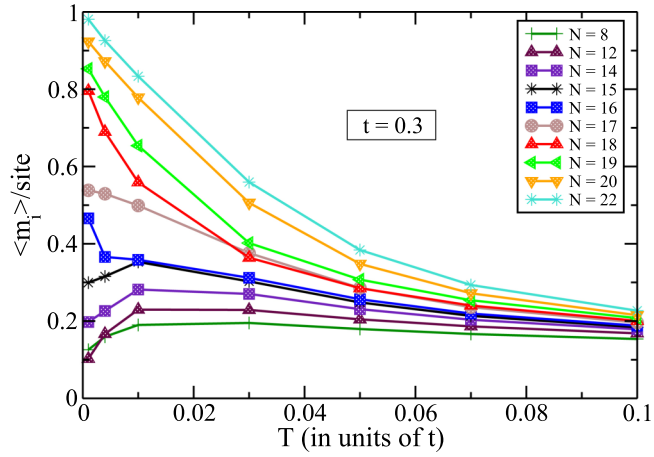


FIG. 9. Averaged per-site total magnetization $\langle m_i \rangle$ (of spins normalized to unity) as a function of temperature (expressed in units of hopping parameter $t$) for a $6 \times 12$ lattice and for various hole densities. The background spin configuration is A-AFM type with hopping $t = 0.3$ eV.

dominant; thus, magnetism in the system increases with increasing temperature. For higher temperatures $T > J_{xy}$ and again at low concentrations (i.e., $x \leqslant 12/72$), the effect of the ferromagnetic coupling $J_{xy}$ also diminishes, and the magnetism decreases with increasing temperature.

#### *1. $t = 0.3$ eV case*

As the concentration of holes increases, initially NNNN interactions and later NNN interactions become relevant; the NN interactions being the strongest are still avoided. Thus, longer ferromagnetic chains are formed, thereby increasing the total magnetization of the system. So by $x = 14/72 \simeq 0.194$ [see Fig. 7(b)], magnetization for lower temperatures such as $T = 0.001t$ starts rising sizably; the peak magnetization value is now at a reduced temperature of $T = 0.01t$ as shown in Fig. 8. By $x = 18/72 = 0.25$ [see Fig. 7(d)] NNN interactions also appear, the different local magnetic polarons start interacting with one another and hence form larger magnetic polarons, and the peak magnetization temperature reduces to $T = 0.001t$; here, starting from $T = 0.1t$, the magnetization increases with decreasing temperature. It is to be noted that there occurs a narrow crossing region ($14/72 \leqslant x \leqslant 17/72$) where magnetization curves for different temperatures intersect. In the crossing regime, there is a complex interplay of various competing effects: (1) aligning of different magnetic polarons due to dominance of $J_{xy}$ over $J_z$; (2) reduction of electron-hole spin interactions due to appearance of NNNN and NNN interactions (of strength $\frac{t^2}{2E_p+4V_p}$); (3) commencing of percolation effects of magnetic polarons due to large hole concentrations; and (4) disordering effects of the temperature. At $x = 18/72$ ($= 0.25$), percolation effect of magnetic polarons is largely dominant over antiferromagnetic interactions. At even higher hole concentrations, this effect is even more pronounced; magnetization rises faster with lowering of temperature. As can be seen from Fig. 8, at lower temperatures and for $x > 15/72$, the magnetization increases faster with increasing hole concentration. At $T = 0.001t$, we get an almost fully ferromagnetic large cluster for $x = 22/72 \simeq 0.3$ [see Fig. 7(e)], with averaged magnetization values close to the maximum possible.

To have an idea about the onset of percolation, we plot in Fig. 9 the magnetization of the system as a function of temperature at fixed hole densities. It appears that the lower-hole-density curves show a magnetization that at first increases and then decreases as the temperature is reduced. It is observed that there is a finite value of magnetization (between 0.15 and 0.2) even at very low densities where holes are noninteracting. A possible explanation for this is that even when no superexchange interactions are considered and when only very few holes are present, magnetization has been tested to decrease as $\frac{1}{\sqrt{N}}$, where $N$ is the total number of sites in the system. Hence, for an A-AFM background, due to the ferromagnetic interaction $J_{xy}$, the fall in magnetization with increasing system size is much slower; however, the magnetization is expected to go to zero for large-sized systems. For $t = 0.3$ eV, around $x \geqslant 16/72$, percolation starts and this is definitely more detectable from the curves depicting $\langle m_i \rangle$/site versus $T$ (see Fig. 9) rather than the plots with $\langle m_i \rangle$/site versus number of holes (see Fig. 8). It is to be noted that the isolated magnetic polarons (that are formed because holes polarize nearest-neighbor particles) get connected to each other by the ferromagnetic layers of the A-AFM and hence percolate. However, the localization length for the carriers (since they are site localized) is always smaller than the size of the magnetic polarons. Hence, electrical conduction is negligible. For hole densities greater than the percolation threshold, at lower temperatures, all curves show an upward rise in the magnetization value; this clearly distinguishes them from the lower-hole-density curves that show a downward trend which for large systems should yield zero magnetization. It is to be noted that for $t = 0.3$ eV, $J_{xy} \simeq 0.02t$ and for $T = 0.05t$, there is a probability $\exp -0.02t/0.05t$ (with $k_B = 1$) that higher-energy values are chosen based on the competition between $J_{xy}$ and $T$. Thus, by $T \geqslant 0.07t$, when the effects of $J_{xy}$ and $J_z$

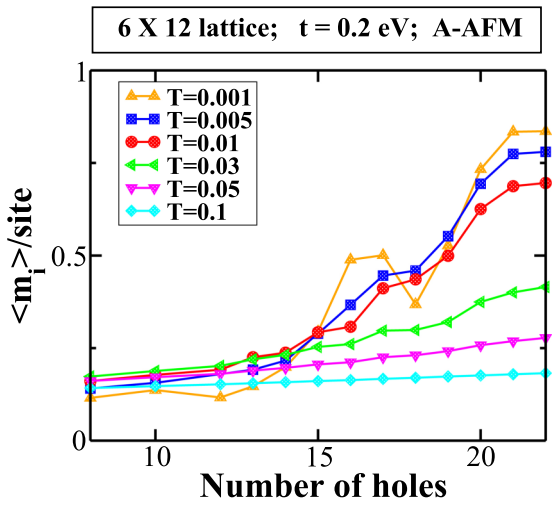


FIG. 10. Averaged per-site total magnetization $\langle m_i \rangle$ (of spins normalized to unity) as a function of the number of holes doped for a $6 \times 12$ lattice and for various temperatures (in units of hopping $t$). The background spin configuration is A-AFM and $t = 0.2$ eV.

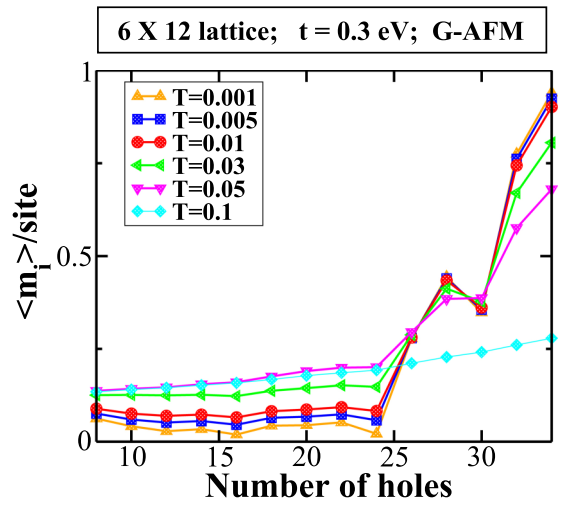


FIG. 11. Averaged per-site total magnetization $\langle m_i \rangle$ (of spins normalized to unity) as a function of the number of holes doped for a $6 \times 12$ lattice and for various fixed temperatures (in units of hopping parameter $t$). The background spin configuration is G-AFM type with $t = 0.3$ eV.

are mostly gone, the system gradually stops percolating. This conclusion is justified since the higher-hole-density curves merge with the lower-density curves (that are essentially noninteracting configurations of particles that do not percolate).

#### *2. $t = 0.2$ eV case*

For the $t = 0.2$ eV situation, the crossing region (i.e., $13/72 \leqslant x \leqslant 19/72$) is wider than it is for the $t = 0.3$ eV case. The peak-magnetization temperature oscillates in the crossing regime (see Fig. 10); furthermore, the curves corresponding to $T \lesssim J_z = 0.024t$ intersect more than once in the crossing region. A plausible explanation for this can be given as follows. The ratio of electron-hole spin interaction and antiferromagnetic coupling $[(\frac{t^2}{2E_p+2V_p})/J_z]$ is only 8; when NNN and NNNN interactions are relevant, the ratio reduces to $(\frac{t^2}{2E_p+4V_p})/J_z = 7$. Thus, antiferromagnetic coupling becomes more prominent than for the the $t = 0.3$ eV case and frustration effects become relevant. It could be due to frustration that, at lower temperatures (such as $T = 0.001t$), the magnetization curve drops at the higher carrier concentration $x = 18/72 = 0.25$. This also could be an indication of the superspin glass phase claimed in experiments [27]; here, "superspin" refers to a spin cluster (i.e., a large magnetic polaron). At $x \geqslant 20/72$ ($\simeq 0.28$), percolation effect of magnetic polarons dominates over antiferromagnetic interactions; magnetization rises with lowering of temperature. Finally, for the higher-hole concentration $x = 22/72 \simeq 0.3$ and at $T = 0.001t$, we get a reasonably high magnetization value of 0.85.

### B. G-AFM background, $t = 0.3$ eV case

To gain further insight, we study the interplay between the strong ferromagnetic electron-hole interaction that polarizes the NN spins of a hole and the superexchange NN antiferromagnetic interaction $J_z$. The magnetic profile, away from the holes, resembles that of a G-AFM system; the holes form ferromagnetic polarons involving the hole spin and the NN spins. At temperatures $T \lesssim J_z = 0.016t$ and hole fillings up to $x = 24/72$, due to the effect of antiferromagnetic $J_z$ coupling on all sides, the polarizations of the magnetic polarons oppose each other, leading to a low magnetization as shown in Fig. 11. For higher temperatures, due to the dominance of the disordering effect of the temperature over the superexchange interaction, there is a probability for the clusters to get less misaligned. Hence, we notice an increase in the magnetization for $T > J_z$. For $x = 24/72 = 1/3$, we have a diagonal stripe order as depicted in Fig. 7(f); each column has two holes. For this arrangement, diagonals containing holes are ferromagnetic, but every such diagonal (with holes) is antiferromagnetically coupled to its neighboring diagonal. In each column, half the spins are in one direction while the other half are in the opposite direction, leading to a very small total magnetization.

Here too, very similar to the case of $t = 0.2$ eV with A-AFM background, there is a crossing region; the crossing occurs in the region $24/72 < x < 32/72$. In the crossing regime, the peak-magnetization temperature oscillates and the curves for $T \lesssim Jz$ intersect thrice in the crossing region. Since all the background spins interact antiferromagnetically (which is in contrast to the A-AFM case), percolation of magnetic polarons dominates over antiferromagnetic interactions at an even larger filling; around $x \geqslant 32/72 = 0.44$ [refer Fig. 7(g)], magnetization increases with lowering of temperature. It is to be noted that, for half-filling [see Fig. 7(h)], we should expect a fully ferromagnetic spin profile with a checkerboard charge structure [28].

### C. Fully FM background, $t = 0.3$ eV

Lastly, to better appreciate subtleties pertaining to FMI, we also study the case where the superexchange interaction is fully ferromagnetic (FM) with coupling $J_z = 0.016t$ when $t = 0.3$ eV. Here, while in the NN vicinity of a hole the spins get strongly polarized, thereby forming a ferromagnetic

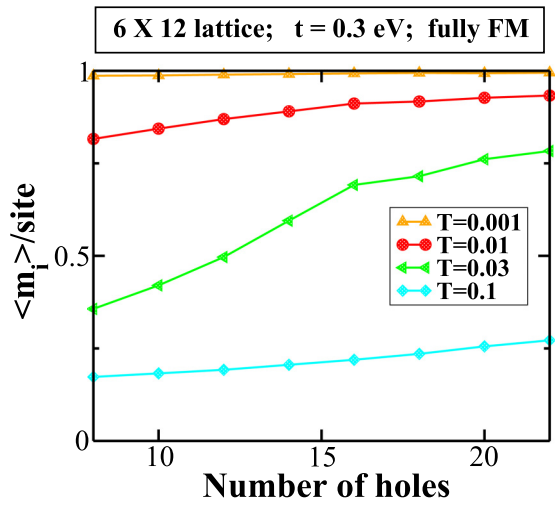


FIG. 12. Averaged per-site total magnetization $\langle m_i \rangle$ (of spins normalized to unity) as a function of the number of holes doped for a $6 \times 12$ lattice and for various fixed temperatures (in units of hopping parameter $t$). The background spin configuration is fully FM and $t = 0.3$ eV.

magnetic polaron, the magnetic profile is that of a weaker FM system away from the holes. Hence, for temperatures much smaller than $J_z$ (such as $T = 0.001t$), we have an almost fully ferromagnetic system as shown in Fig. 12. On increasing the temperature, the spins get more misaligned and the magnetization reduces. At lower fillings, as the temperature increases to the value $0.03t$ (i.e., $T \approx 2J_z$), the disordering effect is large enough so that the magnetization drops considerably as shown in Fig. 12. On the other hand, at higher fillings and again at $T = 0.03t$, percolation of magnetic polarons counters the disordering effect and generates higher magnetization values. For still higher temperatures (such as $T = 0.1t$), the magnetic polarons tend to orient in random directions because the superexchange coupling is ineffective, thereby reducing the magnetization significantly. It is interesting to note that, in all the three Figs. 8, 11, and 12 plotted at $t = 0.3$ eV, the magnetization curves are similar for $T = 0.1t$ because the superexchange is ineffective and hence the nature of superexchange coupling is irrelevant.

## V. CONCLUSIONS AND PERSPECTIVES

We studied the nature of ferromagnetic insulator in the experimentally relevant doping regime of $0.1 \leqslant x \leqslant 0.3$ in bulk manganites. The magnetic interaction considered here applies to manganites with low density of localized holes. In regions without holes, as in the undoped manganites, the magnetic interaction is A-AFM; in a region with a hole, the site-localized hole produces strong ferromagnetic coupling between its spin and its NN electron spins. We find that near the doping $x = 0.3$, the insulator is almost fully ferromagnetic. Now, the critical doping at which the system becomes fully ferromagnetic depends on the dimension; in 2D it is expected to be around twice the value of the critical doping in three dimensions (3D) for the following reason. In a conducting-site percolation problem, the critical concentration for conduction in a simple cubic lattice is 0.31 and in a square lattice it is 0.59 (see Ref. [29]); hence, the critical doping to produce a percolating cluster that is a checkerboard charge-ordered region is $0.5 \times 0.31$ in 3D and at $0.5 \times 0.59$ in 2D see Ref. [30]).

It was experimentally observed that an FMI phase is manifested in the wide-band manganite $La_{1-x}Sr_xMnO_3$ in the doping region $0.1 \lesssim x \lesssim 0.18$ [31], in the intermediate-bandwidth $La_{1-x}Ca_xMnO_3$ in the doping range $0.1 \leqslant x \leqslant 0.225$ [31,32], and in the narrow-bandwidth $Pr_{1-x}Ca_xMnO_3$ in the region $0.1 \leqslant x \leqslant 0.3$ [31]. The fact that the FMI region persists until a higher doping when bandwidth decreases (and concomitantly electron-phonon coupling increases [16]) is consistent with the fact that the tendency to localize increases as bandwidth decreases [18,19]. The hopping values considered in this work are pertinent to wide-bandwidth and intermediate-bandwidth manganites. While our one-band model (involving site-localized holes) is relevant to understand manganites in the FMI region, it is certainly not valid to study the ferromagnet metallic (FMM) phase that occurs at higher doping in manganites; to understand the FMM region, we need to invoke a two-band model and analyze the effect of disorder on localization.

The experimental managanite phase diagram reported in Ref. [33] reveals increasing $T_c$ values at higher dopings for the FMI phase in $La_{1-x}Sr_xMnO_3$. Based on this phase diagram, for a fixed $T < T_c(x = 0.1)$, we expect the magnetization to increase when the doping increases in the FMI region; this is consistent with the curves in Fig. 8. Furthermore, in Fig. 9, a constant magnetization line, such as that of $\langle m_i \rangle$/site $= 0.4$, intersects the constant-hole density curves at larger $T$ values when hole dopings are larger. Thus, $T_c$ increases with increasing $x$. This supports the behavior of $T_c$ in the experimental phase diagrams depicted in Refs. [5,6]. The nature of the phase transition, as can be inferred from Fig. 6, is a second-order phase transition with no visible change in the nature of the magnetic transition even for a larger system size; this agrees with Ref. [13]. Now the nature of the transition is expected to be the same whether temperature is varied (as in Fig. 8) or density is varied (as in Fig. 6).

Next, comparing the $t = 0.2$ eV, A-AFM case with the $t = 0.3$ eV, G-AFM case, we conclude that the antiferromagnetic coupling $J_z$ plays the important role of causing frustrations in the system. We also point out the possible occurrence of glassiness in the system to explain the multiple intersections of the curves in the crossing regime at $T \lesssim J_z$ (see Figs. 10 and 11). Such a picture is supported by the observed superspin glass phase in $La_{0.82}Ca_{0.18}MnO_3$ ferromagnetic insulator at $T \lesssim 70$ K [27]. Further theoretical analysis is required to clearly identify and characterize a superspin glass phase at lower temperatures.

Regarding the transport properties of the system, since we work with a localized band of polarons, the mobility of the polarons is due to activated transport (where electrons can only hop to neighboring sites). The resistivity $\rho$ is thus given as (see Ref. [34])

$$\frac{4\pi}{n_c q_e^2 a^2 \rho} = \beta\omega_0 \left(1 + \frac{M^2}{M_S^2}\right) \exp\left[-2g^2 \tanh\left(\frac{\beta\omega_0}{4}\right)\right], \quad (14)$$

where $M$ is the magnetization, $M_S$ is the saturation magnetization, $a$ is the lattice constant, $q_e$ is the electronic charge, $n_c$ is the density of carriers, and $\beta = \frac{1}{k_B T}$. Now, when an external magnetic field is switched on, this further aligns the spins and hence resistivity of the system drops. This drop in resistivity with the application of an external magnetic field can account for the observed magnetoresistance behavior in the system (see Ref. [13]).

We also would like to make a few observations regarding inclusion of long-range Coulomb (lrc) interaction and the bulk transition from a FMI to a ferromagnetic metal (FMM). Inclusion of lrc interaction can be done in a two-band model to account for inhomogeneities in doped manganites (see Ref. [35]). Localized $l$ states (with Jahn teller energy $E_{\rm JT}$) and undistorted, extended $b$ states (with zero site energy and hopping energy $t$) get acted upon by lrc interaction. They produce, at low doping, distinct regions of unoccupied $b$ states; at intermediate doping, puddles of $b$ states with $l$ polarons as background; finally, at higher doping, percolating $b$ states. However, for small values of doping $x$, because of strong Hubbard $U$, the $b$ states remain away from the polaronic $l$ states thereby reducing the effective bandwidth to $\mathrm{BW}_{\rm effective} = \sqrt{x}\,\mathrm{BW}$. Thus, for small $x$, primarily the region of the ferromagnetic insulator (FMI) which we are focusing on, the $b$ bands are practically empty and the $b$-band bottom is above the polaronic energy $E_{\rm JT}$. Hence, this justifies the use of a one-band model, which is the band of localized polarons in our problem. The inclusion of the lrc interaction is thus not relevant in this case since we want to study, as a function of hole doping, the onset of FMI phase and the effect of temperature on the magnetism of the system. It is also to be noted that, though the transition from an insulator to a metal phase has been explained in Refs. [18,35], a proper treatment of the FMI phase is missing in these works. A detailed treatment of the FMI phase is the primary highlight of our work. We point out that extension of our work to two bands and considering lrc interaction will likely elucidate the FMI-FMM transition; however, this is both analytically and numerically challenging and can be considered as a separate work.

We close by noting that there exist interesting pictures pertaining to charge disproportion (where on adjacent sites $d^4{+}d^4 \longrightarrow d^3{+}d^5$ or $\mathrm{MnO}_6^{9-} + \mathrm{MnO}_6^{9-} \longrightarrow \mathrm{MnO}_6^{8-} + \mathrm{MnO}_6^{10-}$) leading to formation of electron-hole (EH) dimers; this then leads to an EH Bose liquid (see Ref. [36]). However, to have a reasonable theory based on such a Bose liquid, a detailed numerical analysis is needed to demonstrate emergence of a ferromagnetic insulator phase at small doping.

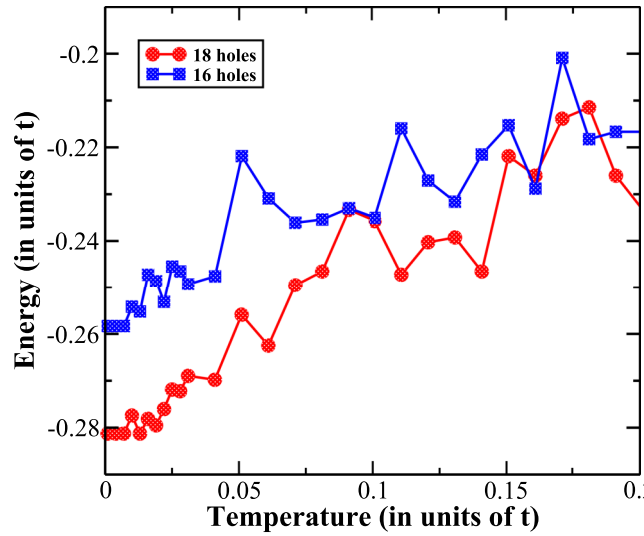


FIG. 13. Averaged total energy per site, as a function of temperature (in units of hopping parameter $t$) for two different hole numbers for a $6 \times 12$ lattice, showing how annealing guides the system to the lowest-energy state. Annealing-based optimized charge configurations are obtained for hopping $t = 0.3$ eV.


## ACKNOWLEDGMENT

The authors thank A. Ghosh, P. B. Littlewood, P. Majumdar, and D. D. Sarma for useful discussions.


## APPENDIX: QUALITY OF ANNEALING IN THE SYSTEM

Showing some of the energetics in the Monte Carlo simulations (as a function of temperature) will also help in understanding the quality of annealing used to obtain optimized charge configurations of the system. It is visible from Fig. 13 that, as temperature is lowered, the system accesses lower-energy states (avoiding possible local minima in the energy landscape); below $T \simeq 0.01t$, the averaged total energy of the system saturates.


[1] D. P. DiVincenzo, J. Appl. Phys. **85**, 4785 (1999).

[2] *Colossal Magnetoresistance, Charge Ordering, and Related Properties of Manganese Oxides*, edited by C. N. R. Rao and B. Raveau (World Scientific, Singapore, 1998).

[3] D. I. Khomskii, Phys. Scr. **72**, CC8 (2005).

[4] T. Hotta, Rep. Prog. Phys. **69**, 2061 (2006).

[5] Y. Tokura, Rep. Prog. Phys. **69**, 797 (2006).

[6] See K. H. Kim, M. Uehara, V. Kiryukhin, and S.-W. Cheong, in *Colossal Magnetoresistive Manganites*, edited by T. Chatterji (Kluwer Academic, Dordrecht, 2004).

[7] C. Martin, A. Maignan, M. Hervieu, and B. Raveau, Phys. Rev. B **60**, 12191 (1999).

[8] A. J. Millis, P. B. Littlewood, and B. I. Shraiman, Phys. Rev. Lett. **74**, 5144 (1995).

[9] S. Kumar and P. Majumdar, Phys. Rev. Lett. **96**, 016602 (2006); arXiv:cond-mat/0406082.

[10] A. Ghosh and S. Yarlagadda, Phys. Rev. B **96**, 125108 (2017).

[11] P. C. Dai, J. A. Fernandez-Baca, E. W. Plummer, Y. Tomioka, and Y. Tokura, Phys. Rev. B **64**, 224429 (2001).

[12] P. C. Dai, J. A. Fernandez-Baca, N. Wakabayashi, E. W. Plummer, Y. Tomioka, and Y. Tokura, Phys. Rev. Lett. **85**, 2553 (2000).

[13] W. Jiang, X. Z. Zhou, G. Williams, R. Privezentsev, and Y. Mukovskii, Phys. Rev. B **79**, 214433 (2009).

[14] V. Markovich, E. Rozenberg, A. I. Shames, G. Gorodetsky, I. Fita, K. Suzuki, R. Puzniak, D. A. Shulyatev, and Y. M. Mukovskii, Phys. Rev. B **65**, 144402 (2002).
[15] V. Markovich, I. Fita, R. Puzniak, M. I. Tsindlekht, A. Wisniewski, and G. Gorodetsky, Phys. Rev. B **66**, 094409 (2002).
[16] T. F. Seman, K. H. Ahn, T. Lookman, A. Saxena, A. R. Bishop, and P. B. Littlewood, Phys. Rev. B **86**, 184106 (2012).
[17] G. G. Guzmán-Verri, R. T. Brierley, and P. B. Littlewood, Nature (London) **576**, 429 (2019).
[18] G. V. Pai, S. R. Hassan, H. R. Krishnamurthy, and T. V. Ramakrishnan, Europhys. Lett. **64**, 696 (2003); T. V. Ramakrishnan, H. R. Krishnamurthy, S. R. Hassan, and G. Venketeswara Pai, Phys. Rev. Lett. **92**, 157203 (2004).
[19] M. Yu. Kagan, D. I. Khomskii, and M. V. Mostovoy, Eur. Phys. J. B **12**, 217 (1999).
[20] P.-G. de Gennes, Phys. Rev. **118**, 141 (1960).
[21] Y. A. Izyumov and Y. N. Skryabin, Phys.-Usp. **44**, 109 (2001).
[22] R. Pankaj and S. Yarlagadda, Phys. Rev. B **86**, 035453 (2012).
[23] A. Dey, M. Q. Lone, and S. Yarlagadda, Phys. Rev. B **92**, 094302 (2015).
[24] P. W. Anderson, Phys. Rev. **115**, 2 (1959).
[25] K. Hirota, N. Kaneko, A. Nishizawa, and Y. Endoh, J. Phys. Soc. Jpn. **65**, 3736 (1996); F. Moussa, M. Hennion, J. Rodríguez-Carvajal, H. Moudden, L. Pinsard, and A. Revcolevschi, Phys. Rev. B **54**, 15149 (1996); G. Biotteau, M. Hennion, F. Moussa, J. Rodríguez-Carvajal, L. Pinsard, A. Revcolevschi, Y. M. Mukovskii, and D. Shulyatev, *ibid.* **64**, 104421 (2001).
[26] N. N. Kovaleva, A. M. Oleś, A. M. Balbashov, A. Maljuk, D. N. Argyriou, G. Khaliullin, and B. Keimer, Phys. Rev. B **81**, 235130 (2010).
[27] P. A. Kumar, R. Mathieu, P. Nordblad, S. Ray, O. Karis, G. Andersson, and D. D. Sarma, Phys. Rev. X **4**, 011037 (2014).
[28] S. Paul, R. Pankaj, S. Yarlagadda, P. Majumdar, and P. B. Littlewood, Phys. Rev. B **96**, 195130 (2017).
[29] A. L. Efros, *Physics and Geometry of Disorder* (Mir Publishers, Moscow, 1986).
[30] S. Datta and S. Yarlagadda, Quantum phase transition in the Holstein model, in *Proceedings of the DAE Solid State Physics Symposium*, edited by K. G. Bhushan, V. K. Aswal, and J. V. Yakhmi (Prime Time Education, Mumbai, 2005), Vol. 50, p. 605.
[31] V. Markovich, A. Wisniewski, and H. Szymczak, Magnetic properties of perovskite manganites and their modifications, in *Handbook of Magnetic Materials*, edited by K. H. J. Buschow (Elsevier, New York, 2014), Vol. 22, pp. 1–201.
[32] P. Schiffer, A. P. Ramirez, W. Bao, and S.-W. Cheong, Phys. Rev. Lett. **75**, 3336 (1995).
[33] A. Urushibara, Y. Moritomo, T. Arima, A. Asamitsu, G. Kido, and Y. Tokura, Phys. Rev. B **51**, 14103 (1995).
[34] S. Yarlagadda, Phys. Rev. B **62**, 14828 (2000).
[35] V. B. Shenoy, Tribikram Gupta, H. R. Krishnamurthy, and T. V. Ramakrishnan, Phys. Rev. Lett. **98**, 097201 (2007); Phys. Rev. B **80**, 125121 (2009).
[36] A. S. Moskvin, Phys. Rev. B **79**, 115102 (2009).